Effect of Aluminum on the Nature of the Iron Species in Fe-SBA-15

Ying Li,† Zhaochi Feng,† Hongchuan Xin,† Fengtao Fan,† Jing Zhang,† Pieter C. M. M. Magusin,‡ Emiel J. M. Hensen,‡ Rutger A. van Santen,‡ Qihua Yang,*,† and Can Li*,†

State Key Laboratory of Catalysis, Dalian Institute of Chemical Physics, Chinese Academy of Sciences, Dalian 116023, China, and Schuit Institute of Catalysis, Eindhoven University of Technology, P.O. Box 513, 5600 MB Eindhoven, The Netherlands

Received: September 5, 2006; In Final Form: October 7, 2006

We report the preparation of highly ordered mesoporous Fe-Al-SBA-15 with isolated extraframework Fe species under acidic conditions. The materials were characterized by means of UV resonance Raman spectroscopy, in conjunction with BET, XRD, TEM, UV−vis, H_2-TPR, FT-IR, and ^{27}Al MAS NMR spectroscopy. The addition of both Fe and Al to the synthesis gel of SBA-15 results in the formation of isolated extraframework Fe species located close to the framework Al ions and the Fe content an order of magnitude higher than that in Fe-SBA-15 synthesized without Al. The existence of anchored extraframework Fe species was confirmed by the presence of a strong absorption band at 270 nm, hydrogen reduction at relatively low temperature, and the presence of a resonance Raman band at 1140 cm^{-1}. The location of Fe in close proximity to framework Al nuclei is further supported by ^{27}Al MAS NMR measurements. Two characteristic UV Raman bands at 510 cm^{-1} and 1090 cm^{-1} excited by 244-nm laser are assigned to Fe−O−Si symmetric and asymmetric stretching modes of isolated tetrahedral Fe ions in the silica framework for Fe-SBA-15. The resonance Raman band at 1140 cm^{-1} excited by 325-nm laser is attributed to the asymmetric stretching mode of the isolated extraframework iron species in Fe-Al-SBA-15. The isolated Fe species close to framework Al species are stable in acidic HCl solution, whereas the majority of Fe species in Fe-SBA-15 can be easily removed.

Introduction

The favorable textural properties of mesoporous silica materials (e.g., M41S, SBA-*n*) make them in principle ideal supports for catalytic conversions of larger reactant molecules[1,2] that cannot diffuse into the micropores of aluminosilicate zeolites. Zeolites have crystalline pore walls ordered at the atomic level and consequently exhibit high ion exchange capacity, which allows facile functionalization of the surface with a suite of transition metal ions such as $Fe^{2+/3+}$, Cu^{2+}, Co^{2+}, and Ni^{2+} by simple and established methods such as ion exchange.[3−8] The highly dispersed catalytic centers are often well-defined and exhibit favorable catalytic properties. The formation of isolated or at least highly dispersed active centers on the surface of mesoporous materials is less straightforward because the amorphous frameworks only exhibit low ion exchange capacity. Conventional techniques for introduction of transition metal ions often lead to surface agglomeration of the metal centers.

Fe-containing HZSM-5 zeolite has been intensively studied because of its promising activity in various reactions such as oxidation of hydrocarbons with nitrous oxide, the decomposition of nitrous oxide, and the selective catalytic reduction of nitric oxide and nitrous oxide in the presence of hydrocarbons or ammonia.[9−28] The nature of the catalytic iron centers remains a moot point with proposals stressing the importance of mononuclear[18−26] and binuclear[19,25] Fe sites having their share of attention. The stabilization of such dispersed Fe centers also remains unclear.[18−28] Recent works suggest the importance of bi- or oligonuclear sites for catalytic nitrous oxide decomposition and of mononuclear sites for selective benzene oxidation.[19,26,27]

Efforts have been made to prepare isolated Fe sites on silica surfaces by grafting of molecular iron species.[29−31] Notably, Nozaki et al. grafted a tri(*t*-butoxy)siloxy iron (III) complex ($Fe[OSi(OtBu)_3]_3(THF)$ to SBA-15.[31] Through controlled calcination, the organic ligands were removed while the mononuclear nature of the complex was retained in the final pseudo-tetrahedral iron oxide cluster. Fe-containing mesoporous silicas such as MCM-41 and MCM-48 synthesized under basic conditions have been reported previously. Fe species in mesoporous materials often exist as isolated tetrahedral Fe, surface Fe oxide clusters, as well as nanosized iron oxides. The isolated Fe species at extraframework positions can hardly be obtained, which are the most interesting active sites in catalysis because of their redox characters.

SBA-15-type mesoporous materials, synthesized under acidic conditions, are attractive because of their higher thermal and hydrothermal stability compared with MCM-type mesoporous materials.[1] However, introducing metal ions such as Fe^{3+} directly into SBA-15 is challenging because of the difficulty of the formation of Fe−O−Si bonds under the strongly acidic synthesis conditions. Previously, we successfully prepared Fe-substituted SBA-15 via a direct hydrothermal method.[32] The Fe species are mainly tetrahedral coordinated in the framework with Fe/Si molar ratios lower than 0.0022. The formation of highly dispersed extraframework Fe species remains a challenge. It has been confirmed that the existence of framework Al species

* Corresponding authors. Telephone: +86-411-8437-9070; 8437-9552. Fax: +86-411-8469-4447. E-mail: canli@dicp.ac.cn; yangqh@dicp.ac.cn.
† Chinese Academy of Sciences.
‡ Eindhoven University of Technology.

10.1021/jp0657641 CCC: $33.50 © 2006 American Chemical Society
Published on Web 12/07/2006

TABLE 1: Physicochemical Properties of Fe-SBA-15, Al-SBA-15, and Fe-Al-SBA-15

samples	Al/Si (molar ratios) gel	Al/Si (molar ratios) product	Fe/Si (molar ratios) gel	Fe/Si (molar ratios) product	Fe/Al (molar ratios)	a_0[a]	surface area (m^2/g)	pore volume (cc/g)	pore diameter[b] (nm)
SBA-15	0	0	0	0		11.6	752	1.35	7.1
Fe-SBA-15[c]	0	0	0.03	0.0007		12.6	902	0.77	6.9
Al-SBA-15[d]	0.05	0.021	0	0		12.5	966	1.17	7.4
Fe-Al-SBA-15 (1)	0.01	0.006	0.03	0.010	1.6	12.8	909	0.94	7.5
Fe-Al-SBA-15 (2)	0.05	0.014	0.03	0.019	1.4	12.5	842	0.89	7.8
Fe-Al-SBA-15 (3)	0.10	0.023	0.03	0.027	1.2	12.1	814	0.92	7.9
Fe-Al-SBA-15 (4)	0.05	0.019	0.01	0.008	0.4	12.5	778	0.57	7.7
Fe-Al-SBA-15 (5)	0.05	0.011	0.05	0.029	2.6	11.4	813	0.64	7.8

[a] a_0 calculated by d_{100} $a_0 = 2 \times d_{100}/\sqrt{3}$ [b] Calculated by the desorption branch of the isotherm according to the BJH method. [c] From ref 32. [d] From ref 48.

has obvious effect on the Fe species in zeolite. Here, we investigate the effect of the simultaneous incorporation of Fe and Al species in mesoporous SBA-15 through the direct synthetic strategy. Specific attention is paid to the effect of Al on the nature of the Fe species in SBA-15.

At present, a suite of techniques (e.g., EXAFS, EPR, Mössbauer, FT-IR, and UV−vis spectroscopy) have been employed to identify the coordination environment of iron in zeolite-based catalysts.[33−36] UV resonance Raman spectroscopy is a powerful technique for the identification of isolated transition metal ions supported on solid matrixes.[37−47] In general, transition metal ions substituted in the framework of mesoporous materials exhibit strong absorption bands in the UV region, which are caused by charge transfer of the framework oxygen anions to isolated transition metal ions. Resonance Raman enhancement can be obtained when an excitation laser is used in this region that meets the appropriate enhancement selection rules.[39,40] Two kinds of vibrations are enhanced: (i) vibrations that are totally symmetric with respect to the absorbing center and (ii) vibrational modes directly involving atoms that undergo the same molecular deformation induced by the electronic excitation. An additional benefit of the use of excitation lines in the UV region is the higher signal-to-noise ratio, because interference by fluorescence of the materials is avoided. In the present work, UV resonance Raman spectroscopy was applied to study the location and coordination environment of Fe ions in SBA-15. Complementary techniques including UV−vis, IR, and NMR spectroscopy will show that Fe species are mainly located in the silica walls in Al-free SBA-15, whereas they occupy pseudo-tetrahedral or octahedral extraframework positions in Al-containing SBA-15.

Experimental Section

Preparation. Fe-SBA-15 and Al-SBA-15 were prepared by direct hydrothermal synthesis as previously reported.[32,48] A typical synthesis process of Fe-Al-SBA-15 samples was as follows: 2 g of P123 surfactant (Aldrich) was dissolved in 70 mL of HCl solution at a pH value of 1.5 (solution A). TMOS (Aldrich, 3.2 mL), an appropriate amount of iron nitrate (Fe/Si molar ratio = 0.01, 0.03, and 0.05), and aluminum isopropoxide (Al/Si = 0.01, 0.05, and 0.10) were mixed with 5 mL of deionized water to obtain solution B. Solution B was stirred at room temperature for ca. 10 min to obtain a clear solution. Then it was added dropwise to solution A. The mixture was stirred vigorously for 20 h at 313 K and was transferred into an autoclave and aged for 24 h at 373 K. The resultant solid was filtered, washed, and dried at 333 K for 15 h. Finally, the as-synthesized mesoporous Fe-Al-SBA-15 was calcined at 773 K for 10 h. The samples are denoted as Fe-Al-SBA-15. The detailed gel composition for Fe-Al-SBA-15 is listed in Table 1. All the characterizations were done with the calcined materials without any pretreatment.

To investigate the stability of Fe species in HCl solution, 0.1 g of sample was added to 200 mL of HCl solution of varying concentration (1, 2, and 3 mol/L). The mixture was stirred at room temperature for 24 h. The solid was finally filtered, washed with distilled water, and dried in an oven at 383 K overnight.

Characterizations. XRD spectra were recorded on a Rigaku D/Max 3400 powder diffraction system using Cu Kα radiation (40 kV and 36 mA) over the range $0.5° \leq 2\theta \leq 10°$. Nitrogen sorption isotherms were determined at 77 K on a NOVA 4200 E system in static measurement mode. Prior to sorption experiments, the samples were outgassed at 573 K for 10 h. The pore size distribution was calculated by analyzing the desorption branch of the isotherm by the Barrett−Joyner−Halenda (BJH) method. Transmission electron microscopy (TEM) micrographs were taken on a JEM-3010 electron microscope (JEOL, Japan) with an acceleration voltage of 300 kV. The elemental composition (Al and Fe) was determined by ICP-AES after the sample was dissolved in a mixture of HF and HNO_3. Diffuse reflectance UV−vis spectra in the range of 200−800 nm were taken on a JASCO V-550 UV−vis spectrophotometer equipped with a diffuse reflectance attachment, using $BaSO_4$ as reference. Temperature-programmed reduction (TPR) was carried out using a mixture of 10 vol % H_2 in He. The catalyst was contained in a quartz tube, treated in a flow of helium at 423 K for 1 h, and cooled at 373 K. TPR was then performed by heating at a rate of 10 K/min to 1273 K in the reducing mixture. The hydrogen consumption was measured by a thermal conductivity detector.

Magic-angle spinning (MAS) ^{27}Al NMR spectra were recorded on a Bruker DMX500 spectrometer equipped with a 4-mm MAS probe head. The ^{27}Al NMR frequency was 130 MHz. The sample rotation speed was 12 kHz. The chemical shifts and excitation angles were calibrated against a saturated $Al(NO_3)_3$ solution. Single-pulse excitation was used with a $\pi/10$ pulse of 1 μs and an interscan delay of 0.1 s. Shortening the excitation pulse did not affect the relative MAS ^{27}Al NMR line shape, while lengthening the interscan delay had no effect on the absolute intensity. The spectra were background-corrected by subtracting the spectrum of the empty sample holder. To compare the total spectral intensity among the various Fe-Al-SBA-15 systems and to their respective element composition, the amount of NMR sample was weighed. All samples were extensively exposed to the same air atmosphere with standard humidity before and during packing of the sample holders.

Infrared spectra of adsorbed pyridine were taken on a Thermo Nicolet NEXUS 470 FT-IR spectrometer. The samples were pressed into self-supporting wafers and were evacuated in a vacuum cell at 673 K for 2 h. Background spectra were recorded

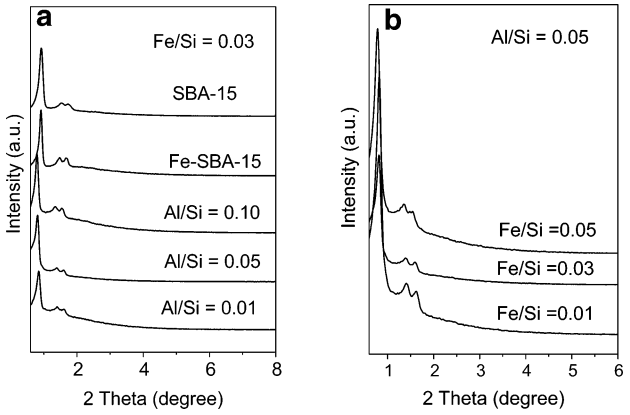

Figure 1. Powder XRD patterns of (a) SBA-15, Fe-SBA-15, and Fe−Al-SBA-15 at an Fe/Si ratio of 0.03 with decreasing Al/Si ratio and (b) Fe-Al-SBA-15 at an Al/Si ratio of 0.05 with decreasing Fe/Si ratio. Note that the M/Si ratios refer to initial gel ratios.

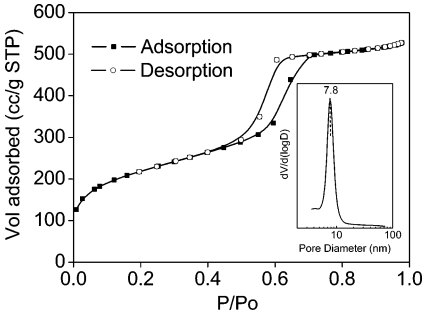

Figure 2. Nitrogen adsorption−desorption isotherm and pore size distribution (inset) for Fe-Al-SBA-15 (Fe/Si = 0.03, Al/Si = 0.05).

after the sample was cooled to room temperature. Pyridine was then admitted to the cell, and the infrared spectra of adsorbed pyridine were recorded after degassing at 423, 523, and 623 K. UV-Raman spectra were collected at room temperature with a Jobin-Yvon T64000 triple-stage spectrograph with a spectral resolution of 2 cm^{-1}. The laser line at 325 nm of a He−Cd laser was used as an exciting source with an output of 25 mW. The power of the laser at the sample was about 3.0 mW. The 244-nm line from a Coherent Innova 300 Fred laser was used as an excitation source in the deep UV region. The power of the 244-nm line at the sample was below 1.0 mW.

Results and Discussion

Mesoporous Structure of the Materials. The powder XRD patterns for Fe-SBA-15 and Fe-Al-SBA-15 are shown in Figure 1. The successful formation of well-ordered mesoporous materials with two-dimensional hexagonal structure follows from the presence of a basal (100) peak along with (110) and (200) reflections in the low-angle region.[1] No typical diffraction peaks due to iron oxide aggregates were observed in the high-angle diffraction range. Compared to SBA-15, the addition of Fe^{3+} to the synthesis gel in Fe-SBA-15 greatly improves the structural order of the resulting material, in agreement with our earlier report.[32] The addition of inorganic salts is beneficial to the long-range order of mesoporous materials,[49] which can be attributed to the specific interaction between the non-ionic surfactant and the metal ions. The improvement is also evident for Fe-Al-SBA-15 mesoporous materials.

The nitrogen sorption isotherm for Fe-Al-SBA-15 (2) is shown in Figure 2. The isotherm is typical for all SBA-15 synthesized in this study. The corresponding textural properties are summarized in Table 1. The isotherm can be classified as type IV with an H1 hysteresis loop, which is common for mesoporous materials with large pores and a narrow pore size distribution.[1,48,50] The well-defined step at relative high pressures of 0.6−0.8 corresponds to the capillary condensation of nitrogen and indicates a narrow pore size distribution. All materials have pore diameters in the range of 6.9−7.8 nm and exhibit surface areas above 750 m^2/g. Transmission electron micrographs of calcined Fe-Al-SBA-15 (2) (Figure 3) confirm the well-ordered hexagonal arrays of one-dimensional mesopores with a diameter close to the one determined from the nitrogen sorption isotherm.

Coordination Environment of Iron. The presence of Al in the synthesis gel provokes a significant increase of the amount of Fe incorporated in the final material (Table 1). The Fe/Si molar ratios (0.010−0.027) are more than 10 times higher than that in Fe-SBA-15 (0.0007) prepared under similar conditions. The Fe content in the final products increases obviously with increase in Al content. Direct synthesis of Fe-substituted SBA-15 with high Fe/Si ratios is difficult due to the low stability of Fe−O−Si bonds under the acidic synthesis conditions.[32] In the present synthesis, Fe and Al are introduced into the synthesis gel. The incorporation of aluminum in SBA-15 is easier than that of iron as shown in Table 1. This difference is due to the smaller ionic radius of Al^{3+}. Noteworthy is the decrease of the final Fe/Al ratios from 1.6 for Fe-Al-SBA-15 (1) to 1.2 for Fe-Al-SBA-15 (3) with increasing Al content. This trend suggests that, although more Fe can be incorporated with increasing Al content in the synthesis gel, a more or less constant number of Fe atoms corresponding to a Fe/Si ratio of 0.005 (0.45 wt %) ends up in the final product independent of the Al content. We surmise that this amount relates to framework Fe^{3+} species. However, in the absence of Al (Fe-SBA-15), the amount of Fe incorporated in the SBA-15 was much lower. Therefore, the incorporation of ferric ions in the framework of SBA-15 appears to be facilitated by the presence of Al^{3+} in the synthesis gel. When the Fe/Si ratio in the gel is lowered to 0.01 (Fe-Al-SBA-15 (4)) at constant Al/Si ratio of 0.05, the resulting Fe/Al ratio is 0.4 compared to a value of 1.2 for Fe-Al-SBA-15 (2). Compared to the latter material, a higher fraction of the iron present in the synthesis gel has been built into the final product.

Figure 4 displays the UV−vis spectra of the calcined Fe-Al-SBA-15. The spectra are dominated by an intense absorption band at 270 nm. This band is assigned to isolated extraframework species in an octahedral or pseudo-tetrahedral environment.[26] The intensity of this band is found to increase with Fe content. This band exhibits a tail in the range of 300−700 nm, which becomes more pronounced with Fe content increasing. A band at 333 nm has been assigned to octahedral Fe ions in oligomeric clusters, while more extensive clustering gives rises to a band in the visible region (427 nm).[9,51] In Fe-Al-SBA-15, a weak shoulder at lower wavelength is visible.

The large difference in the coordination environment of iron in Fe-SBA-15 and Fe-Al-SBA-15 is exemplified by the UV−vis spectra in Figure 5. Fe-Al-SBA-15 shows an intense absorption band around 270 nm. The UV−vis spectrum of Fe-SBA-15 is dominated by absorption bands in the range of 220−245 nm. Clearly, Fe-SBA-15 mainly contains tetrahedral Fe^{3+} species in the framework of SBA-15. Absorption at longer wavelengths is essentially absent for Fe-SBA-15, indicating that this material contains predominantly isolated, tetrahedral framework Fe^{3+} species.

Raman spectroscopy can be used to identify various states of iron species.[18,41,53] Raman bands can be selectively enhanced by the resonance Raman effect, which becomes pronounced when the excitation wavelength is close to an absorbance band

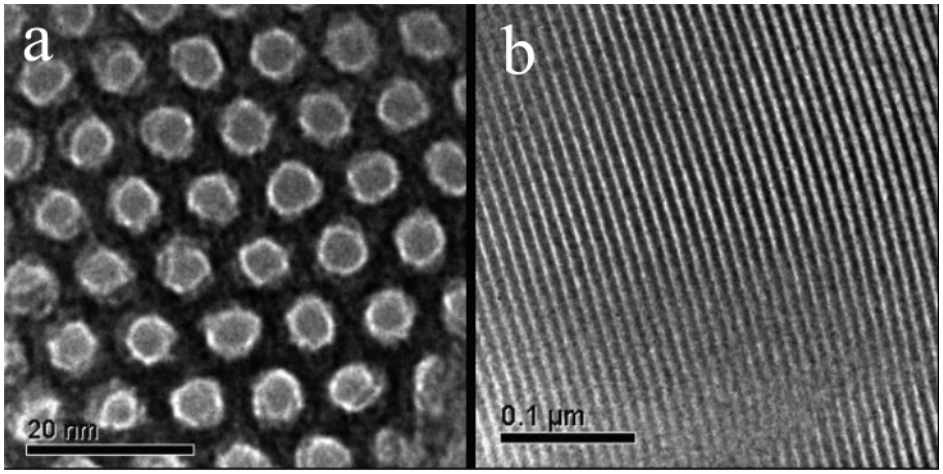

Figure 3. TEM images of Fe-Al-SBA-15 (2) (gel ratios Fe/Si = 0.03, Al/Si = 0.05) viewed (a) in the direction parallel to the pore axis and (b) in the direction perpendicular to the pore axis.

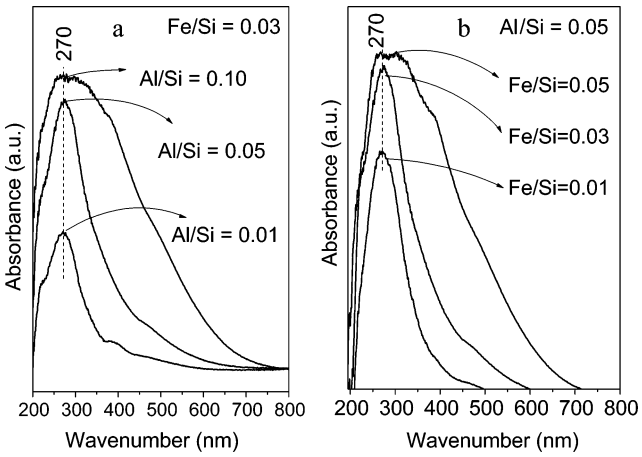

Figure 4. UV−vis absorption spectra of Fe-Al-SBA-15. (a) Fe-Al-SBA-15 with Fe/Si = 0.03; Al/Si = 0.01, 0.05, and 0.10. (b) Fe-Al-SBA-15 with Al/Si = 0.05; Fe/Si = 0.01, 0.03, and 0.05.

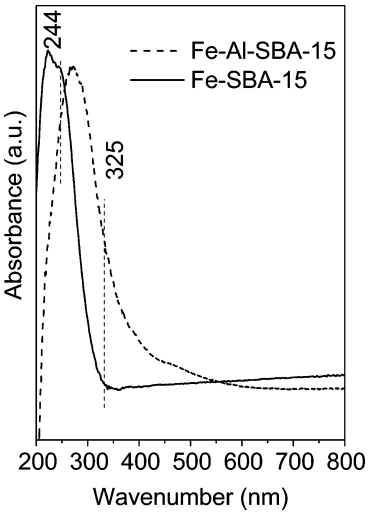

Figure 5. Comparison of UV−vis absorption spectra of Fe-SBA-15 (Fe/Si = 0.03) and Fe-Al-SBA-15 (Fe/Si = 0.03, Al/Si = 0.05). The excitation lines at 244 and 325 nm for the resonance Raman measurements are also indicated.

of the charge-transfer transition, in this case the LMCT transition of $O^{2-} \rightarrow Fe^{3+}$. Figure 5 suggests that the excitation lasers with wavelengths at 244 and 325 nm are able to identify the isolated framework and the isolated extraframework Fe species, respectively.

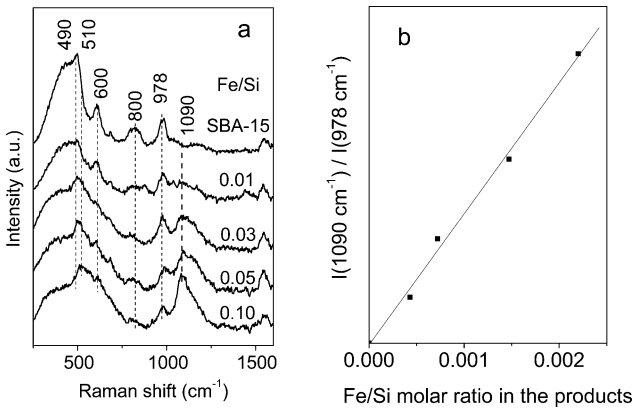

Figure 6. (a) UV resonance Raman spectra of SBA-15 and Fe-SBA-15 with various Fe content excited by the 244-nm line. (b) Plots of the intensity ratios of the band at 1090 cm^{-1} to the band at 978 cm^{-1} vs the Fe/Si molar ratios in the Raman spectra of Fe-SBA-15.

Figure 6a shows the UV resonance Raman spectra of SBA-15 and Fe-SBA-15 with various Fe contents with 244-nm excitation. Four Raman bands at 490, 600, 800, and 978 cm^{-1} are observed for pure siliceous SBA-15. The bands at 490 and 600 cm^{-1} are assigned to the vibration modes of three- and four-membered siloxane rings, respectively, and the band at 800 cm^{-1} is assigned to the stretching mode of the siloxane linkage. The band at 978 cm^{-1} is often associated with the Si−O−Si bond near framework iron species or, in this case, near defect sites such as surface silanol groups.[32,45] Compared to the spectrum for siliceous SBA-15, a new band at 1090 cm^{-1} is detected for Fe-SBA-15. This band is assigned to the Fe−O−Si asymmetric stretching mode of isolated tetrahedral iron ions in the silica framework. The band initially present at 490 cm^{-1} appears to shift to higher frequency when Fe is introduced into SBA-15. This shift is actually due to an additional band of the symmetric Fe−O−Si stretching mode of the isolated tetrahedral iron ions in the silica framework. The intensity of the band at 510 cm^{-1} is stronger than the vibration bands at 490, 600, and 800 cm^{-1} due to the resonance Raman effect. Therefore, the feature at 490 cm^{-1} due to the vibrational band of the siloxane bond is occluded by the stronger band at 510 cm^{-1} in Fe-SBA-15.

Figure 6b plots the intensity ratio of 1090 to 978 cm^{-1} versus the Fe/Si molar ratio of calcined Fe-SBA-15. The intensity ratio of the 1090 cm^{-1} (corresponding to the isolated Fe−O−Si species) and 978 cm^{-1} (the characteristic Raman band of the pure silica SBA-15) bands should be roughly proportional to

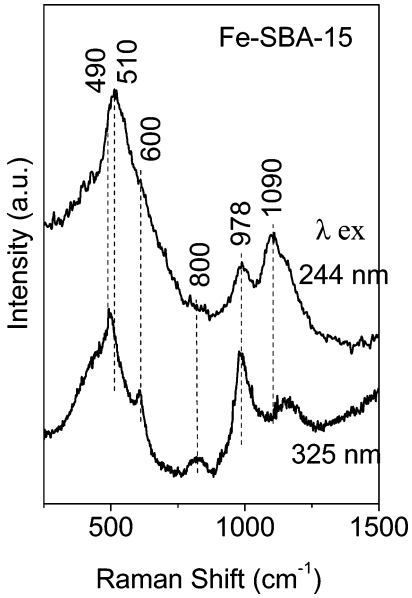

Figure 7. UV resonance Raman spectra of Fe-SBA-15 (Fe/Si = 0.03) excited by 244- and 325-nm laser lines.

the concentration of the isolated framework iron in Fe-SBA-15 when the concentration of iron ion is relatively low. This intensity ratio increases linearly with the Fe/Si molar ratios from 0 to 0.0022. The detailed other characterizations of these Fe-SBA-15 have been reported in our previous work.[32]

Figure 7 compares the resonance Raman spectra of Fe-SBA-15 excited by 244- and 325-nm laser lines. Strong Raman bands at 510 and 1090 cm^{-1} are visible for Fe-SBA-15 using excitation at 244 nm. When the 325-nm laser line is used, there is no resonance Raman enhancement because the frequency is not close enough to that of the corresponding charge-transfer band. Without resonance Raman enhancement, the Raman band related to the Fe−O−Si bond is too weak to be observed because of the very low Fe content. It is clear that the two Raman bands at 510 and 1090 cm^{-1} excited with 244-nm excitaition relate to tetrahedrally coordinated isolated Fe framework species. In correspondence with earlier works reported for titanosilicates and Fe-ZSM-5,[37−39,43] we assign the 1090 cm^{-1} band to the asymmetric stretching mode and the 510 cm^{-1} band to the symmetric stretching mode of tetrahedral coordinated Fe−O−Si bonds.

Resonance Raman spectra of Fe-Al-SBA-15 with Fe/Si ratios of 0.01 and 0.03 with excitation at 325 nm are displayed in Figure 8a. In addition to a weak band at 1080 cm^{-1}, a new band at 1140 cm^{-1} is detected for Fe-Al-SBA-15. The intensity of this band increases with increasing Fe content. The band at 1080 cm^{-1} relates to the framework Fe species. In contrast to Fe-SBA-15, this band becomes more prominent with excitation at 325 nm because of the higher Fe content of Fe-Al-SBA-15. This suggests that the amount of framework Fe species in Fe-Al-SBA-15 is higher than that in Fe-SBA-15, in line with our earlier analysis of the chemical analyses. The band at 1140 cm^{-1} is possibly attributed to extraframework Fe species. To further confirm this assignment, resonance Raman spectra of Fe-Al-SBA-15 excited at 244 and 325 nm are compared in Figure 8b. The band at 1140 cm^{-1} is stronger than the one at 1080 cm^{-1} at 325-nm excitation. However, the band intensities are reversed when 244 nm is used as the excitation laser. This shows that these two resonance Raman bands correspond to different Fe species. Combined with the UV−vis results, the band at 1140 cm^{-1} can therefore be assigned to isolated extraframework Fe species, while the band at 1080 cm^{-1} is attributed to the

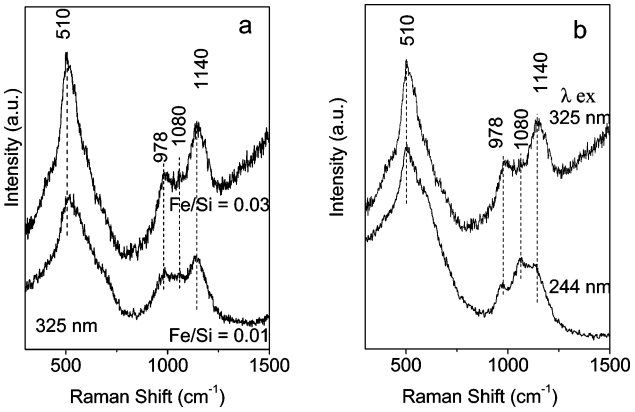

Figure 8. (a) UV resonance Raman spectra of Fe-Al-SBA-15 with various Fe contents excited by 325-nm laser lines. (b) UV resonance Raman spectra of Fe-Al-SBA-15 (Fe/Si = 0.03, Al/Fe = 0.05) excited by 244- and 325-nm laser lines.

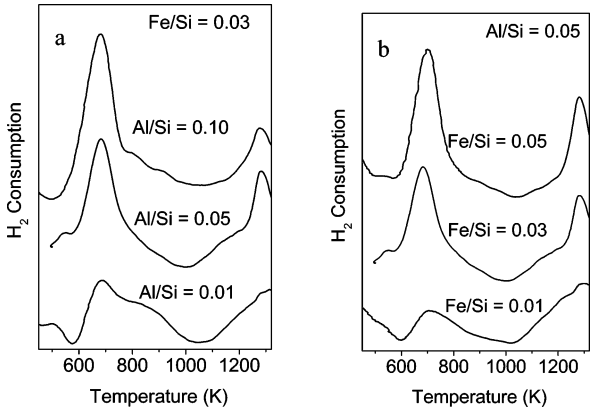

Figure 9. H_2 TPR patterns Fe-Al-SBA-15. (a) Fe-Al-SBA-15 with Fe/Si = 0.03; Al/Si = 0.01, 0.05, and 0.10. (b) Fe-Al-SBA-15 with Al/Si = 0.05; Fe/Si = 0.01, 0.03, and 0.05.

framework Fe species. Notably, the resonance band corresponding to tetrahedral framework Fe species for Fe-Al-SBA-15 shifts slightly from 1090 to 1080 cm^{-1} compared to that of Fe-SBA-15. This may be due to the presence of Al centers in proximity to the framework Fe species, changing the symmetry of the Fe−O stretching mode slightly.

In summary, using selective resonance Raman enhancement, we show that the 510 and 1090 cm^{-1} bands correspond to Fe−O−Si vibrations of tetrahedrally coordinated isolated Fe framework species. We assign the 1090 and 510 cm^{-1} bands to the asymmtric and symmetric stretching modes, respectively. A higher Fe content induced by the presence of Al during synthesis results in the appearance of a band at 1140 cm^{-1} which is selectively enhanced by the use of the 325-nm laser line, from which it follows that this species corresponds to isolated extraframework species, most likely in octahedral coordination.

Figure 9 displays the hydrogen TPR patterns of the Fe-Al-SBA-15. Two distinct reduction peaks at 688 and 1273 K are observed, which are sufficiently separated to allow the identification of at least two distinct types of Fe^{3+} species. The first peak corresponds to the reduction of extraframework Fe^{3+} species, which can easily to be reduced at lower temperature. The reduction temperature is similar to that observed for Fe-silicalite.[52] The second feature is ascribed to Fe^{3+} species in the framework of SBA-15 that are more difficult to be reduced. Clearly, the first reduction peak increases with increasing iron content.

Coordination Environment of Aluminum. Figure 10a shows the ^{27}Al MAS NMR spectra of Al-SBA-15 and Fe-Al-

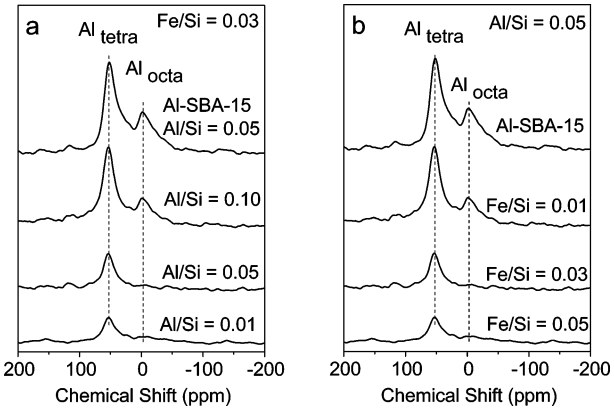

Figure 10. ^{27}Al MAS NMR spectra of Al-SBA-15 and Fe-Al-SBA-15. (a) Al-SBA-15 with Al/Si = 0.05 and Fe-Al-SBA-15 with Fe/Si = 0.03; Al/Si = 0.01, 0.05, and 0.10. (b) Al-SBA-15 with Al/Si = 0.05 and Fe-Al-SBA-15 with Al/Si = 0.05; Fe/Si = 0.01, 0.03, and 0.05.

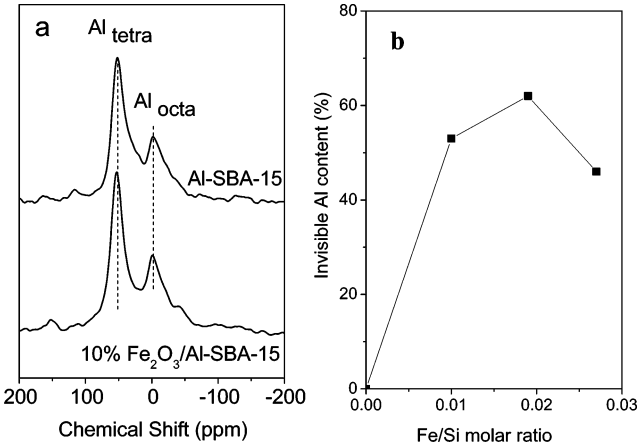

Figure 11. (a) ^{27}Al MAS NMR spectra of Al-SBA-15 and physical mixture of 10 wt % Fe_2O_3 and Al-SBA-15. (b) Fraction of undetected Al as a function of the Fe content in calcined Fe-Al-SBA-15. The fraction was obtained by comparing the total resonant area of Al spectra of Fe-Al-SBA-15 with that of Al-SBA-15.

SBA-15 with different Al contents, and Figure 10b gives the ^{27}Al MAS NMR spectra of Al-SBA-15 and Fe-Al-SBA-15 with different Fe contents. Each spectrum was normalized to the absolute amount of Al. The spectra contain a dominant resonance at 54 ppm assigned to tetrahedrally coordinated Al species.[53] Additionally, the weak resonance at 0 ppm indicates the presence of a small amount of extraframework Al species with octahedral coordination in Al-SBA-15 and Fe-Al-SBA-15.

The normalized signal intensity at 54 ppm is much smaller for Fe-Al-SBA-15 compared with that of Al-SBA-15. Moreover, the resonance at 0 ppm is not observed for materials with higher Fe contents. This is due to the paramagnetism of iron species. The paramagnetic Fe center strongly broadens the resonance of the Al nuclei in their close vicinity and makes the Al signal beyond NMR detection.[20−22] Models have been developed and tested for the effect of paramagnetic ions on NMR relaxation and line broadening in solution, in particular in the context of MRI contrast agents.[54,55] Paramagnetic broadening in solids is different, however, because isotropic rotational motion is absent, and the iron species may not be homogeneously distributed as mononuclear species in the material. In solids, the first-order dipolar broadening is inversely proportional to the cube of the distance between the unpaired electrons and the observed NMR nucleus. As for the NMR visibility of ^{27}Al in a zeolite with supposedly highly dispersed Fe^{3+} cations, a typical Fe−Al distance r_{Fe-Al} is estimated below, in which ^{27}Al MAS NMR signals are invisible from the condition that in these "black-hole" regions the electron−nuclear dipole coupling constant ν_D would be much larger than the sample rotation rate ν_r. Because of the strong first-order dipole coupling, the intensity of the central Al transition would be distributed over many spinning side bands and easily disappears under the spectral noise level. In addition, at large ν_D:ν_r ratios higher-order dipolar broadening effects may occur, which further broaden the NMR signal. For (high-spin) Fe^{3+} with five unpaired electrons in undistorted 3d orbitals, this yields the condition

$$\upsilon_D = \sum_{k=1}^{5} \frac{\mu_0 \gamma_{Al} \gamma_e}{8\pi^2 r_{Al-e}{}^3} >> \upsilon_r$$

where γ_e and γ_{Al} are the gyromagnetic ratios for electrons and ^{27}Al nuclei, respectively; μ_0 is the permeability constant; and r_{Al-e} is the respective electron−Al distances, which for long distances equal the Fe−Al internuclear distance. Inserting a sample rotation rate ν_r of about 10 kHz, we obtain a typical boundary distance of 2 nm. Because of the cube-distance dependence, this value is not very sensitive to the exact value of the MAS rate. Thus, all ^{27}Al nuclei within a 2-nm sphere around a Fe^{3+} cation would be hardly detectable in MAS ^{27}Al NMR.

Thus, the NMR invisibility of some ^{27}Al nuclei indicates the presence of Fe near Al cations. To prove that this paramagnetic broadening is really a close-distance interaction indeed, we have also recorded the ^{27}Al MAS NMR spectra of physical mixtures of iron oxide and Al-SBA-15 with a similar overall Fe/Al/Si content (Figure 11a). The resulting normalized intensity of this physical mixture is almost similar to that of the Al-SBA-15 materials. It is not easy to determine for Fe-Al-SBA-15 whether all Al atoms are in tetrahedral framework positions or whether some of them are at extraframework position, because the Fe^{3+} ions may also be located close to extraframework octahedral Al sites. Figure 11b plots the fraction of invisible Al in the Fe-Al-SBA-15 materials as a function of the Fe content. This fraction is calculated from integration of the resonant areas of the contribution at chemical shifts of 0 and 54 ppm of the normalized spectra. The contribution of invisible ^{27}Al nuclei clearly increases with Fe content and goes through a maximum. The decrease at the highest Fe content agrees with the earlier observation of an increased contribution of clustered iron oxide species in the UV−vis spectra. Clearly, such nanometer-sized, aggregated iron oxide phases will be more distant from the ^{27}Al nuclei.

Stability of Fe Species of Fe-SBA-15 and Fe-Al-SBA-15 in HCl Solution. It is well-known that iron oxide species dispersed over a silica surface leach easily in acidic solutions. To investigate the stability of surface-bound Fe species in the various materials, Fe-SBA-15 and Fe-Al-SBA-15 were treated in HCl solutions with varying concentrations at room temperature. Figure 12 gives the resonance Raman spectra of Fe-SBA-15 and Fe-Al-SBA-15 after this treatment. For Fe-SBA-15, the resonance Raman band at 1090 cm^{-1} is decreased considerably, indicating that a large part of the framework Fe species is removed by the acid treatment, accompanying an increase in the band at 978 cm^{-1}. This is possibly due to the dissolution of silica species, resulting in the formation of defect sites and silanol groups.[45] In contrast, for Fe-Al-SBA-15 the intensities of the resonance Raman bands at 1080 and 1140 cm^{-1} are not decreased, but the signal-to-noise ratio slightly increased after

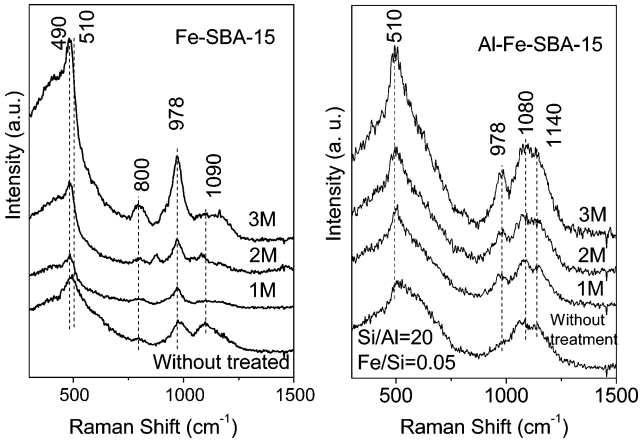

Figure 12. UV resonance Raman spectra of Fe-SBA-15 and Fe-Al-SBA-15 treated in HCl solutions with various concentrations for 24 h excited by the 244-nm laser line.

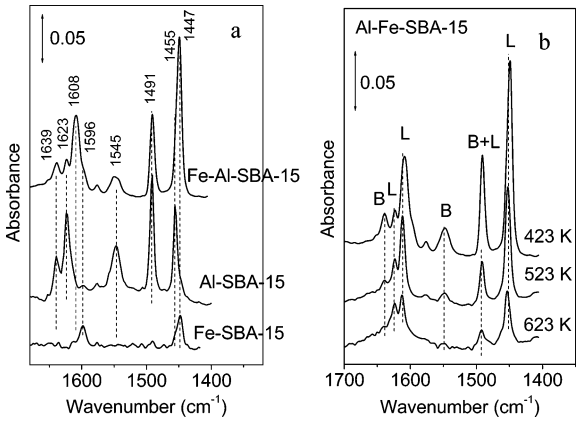

Figure 13. (a) Room-temperature infrared spectra of adsorbed pyridine for Fe-SBA-15 (Fe/Si = 0.03), Al-SBA-15 (Al/Si = 0.05), and Fe-Al-SBA-15 (Fe/Si = 0.05, Al/Si = 0.05) after outgassing at 423 K. (b) Room-temperature infrared spectra of adsorbed pyridine for Fe-Al-SBA-15 (Fe/Si = 0.05, Al/Si = 0.05) after outgassing at 423, 523, and 623 K.

the sample was treated in 3 M HCl solution for 24 h. This clearly indicates that the iron species in Fe-Al-SBA-15 is relatively stable against the acid treatment.

As previously reported,[32] Raman spectroscopy with the excitation of UV laser at 244-nm excitation is not sensitive to iron oxides because the Raman scattering in the UV region is adsorbed by the nanosized iron oxide. The highly dispersed iron oxide in mesoporous SBA-15 or Al-SBA-15 absorb the Raman scattering from framework or extraframework Fe species, thus diminishing the total Raman signal intensity of the isolated species in framework or extraframework. The fact that the signal-to-noise ratio of the Raman spectra of the untreated Fe-Al-SBA-15 is worse than that of the HCl treated sample is due to the existence of iron oxide particles as also shown in the UV−vis absorption spectrum of Fe-Al-SBA-15 (5) (Figure 4). This result indicates that the isolated Fe species anchored on the framework Al are stable toward HCl, whereas the extraframework iron species without Al and dispersed iron oxides can be dissolved in acidic solution.

Acidity Probed by Infrared Spectroscopy of Adsorbed Pyridine. The acid sites of Fe-Al-SBA-15 were determined by infrared spectra of adsorbed pyridine. Figure 13a shows the spectra of adsorbed pyridine for Fe-SBA-15 and Fe-Al -SBA-15 after degassing at 423 K. Typical IR bands of adsorbed pyridine for Al-SBA-15 include those related to hydrogen-bonded pyridine (1447 and 1599 cm^{-1}), pyridine adsorbed on Lewis acid sites (1455 and 1623 cm^{-1}), pyridine adsorbed on Brønsted acid sites (1547 and 1640 cm^{-1}), and a band at 1490 cm^{-1} attributed to pyridine associated with both Lewis and Brønsted acid sites.[56,57] Fe-SBA-15 only exhibits infrared bands related to hydrogen-bonded pyridine (1447 and 1599 cm^{-1}), similar to siliceous SBA-15. Clearly, the concentration of Lewis and Brønsted acid sites is very low in Fe-SBA-15 with low content of Fe. Notably, the infrared spectrum of Fe-Al-SBA-15 contains a new band at 1607 cm^{-1} corresponding to different Lewis acid sites compared with Al-SBA-15. Although not conclusive, this band may relate to an isolated Fe^{3+} ion, stabilized by a negatively charged aluminum-occupied oxygen tetrahedron in the SBA-15 pore wall. Figure 13b gives the infrared spectra of adsorbed pyridine on Fe-Al-SBA-15 after degassing at various temperatures. With desorption temperature increasing, the intensities of the bands due to the Brønsted and Lewis acid sites decrease strongly in contrast to the band at 1607 cm^{-1} which remains relatively stable up to temperatures of 623 K.

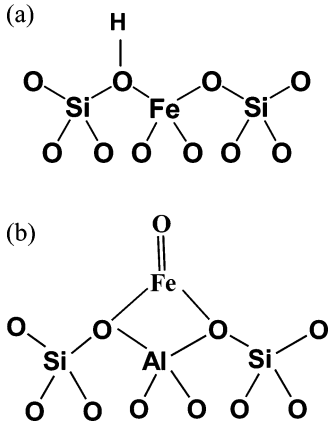

Figure 14. (a) Schematic illustration of isolated framework Fe species in Fe-SBA-15 (UV resonance Raman bands, 1090 and 510 cm^{-1}). (b) Possible schematic illustrations of the extraframework Fe species in Fe-Al-SBA-15 (UV resonance Raman bands at 1140 cm^{-1}).

The Structure of Isolated Fe Species in Fe-SBA-15 and Fe-Al-SBA-15. Summarizing, the simultaneous incorporation of Al and Fe ions in the SBA-15 silica results in the formation of isolated extraframework Fe species in addition to framework Fe species. When Fe-SBA-15 is synthesized in the absence of Al^{3+}, framework Fe^{3+} species are predominant. The extraframework Fe species in Fe-Al-SBA-15 are located near framework Al ions, and the Fe−O−Al bonds may be formed during the condensation reactions during the synthesis. A less likely alternative is the exchange of Fe cations onto the acidic site of the framework Al ion. Figure 14 gives tentative models for the isolated Fe species in Fe-SBA-15 and Fe-Al-SBA-15. Fe-SBA-15 primarily contains tetrahedral framework iron species. The symmetric and asymmetric Fe−O stretching mode in Fe−O−Si species in isolated tetrahedral coordination in the silica gives rise to UV resonance Raman bands at 510 and 1090 cm^{-1} at 244-nm excitation. In Fe-Al-SBA-15, extraframework Fe species are stabilized by tetrahedral framework Al ions. The asymmetric stretching mode of the isolated extraframework iron species gives the UV resonance Raman bands at 1140 cm^{-1} at 325-nm excitation.

Conclusions

Highly ordered SBA-15 materials containing isolated Fe species in framework and extraframework positions were

successfully prepared by direct hydrothermal synthesis. The simultaneous incorporation of Fe and Al leads to an increase of the Fe content in the final mesoporous silica material compared to the aluminum-free case. The isolated extraframework iron ions are stabilized by the tetrahedral framework Al ions. Highly isolated framework and extraframework iron species have been selectively identified by resonance Raman spectroscopy. The framework iron species in Fe-SBA-15 can be identified by their characteristic resonance Raman bands at 1090 and 510 cm^{-1}. The extraframework Fe species in Fe-Al-SBA-15 can be identified by the characteristic resonance Raman band at 1140 cm^{-1} excited by a laser at 325 nm. Further support for the structural differences between Fe-SBA-15 and Fe-Al-SBA-15 is provided by UV−visible diffuse reflectance spectroscopy, hydrogen TPR, ^{27}Al MAS NMR spectroscopy, and pyridine adsorbed IR spectroscopy measurements. The highly isolated cationic Fe species in Fe-Al-SBA-15 is stable even in 3 M HCl solutions, because the isolated Fe species are stabilized by nearby framework Al ions.

Acknowledgment. This work was financially supported by the National Basic Research Program of China (Grant Nos. 2003CB615806 and 2003CB615803), National Natural Science Foundation of China (NSFC Grant Nos. 20321303 and 20273069), and the Program for Strategic Scientific Alliances between China and The Netherlands funded by the Royal Netherlands Academy of Arts and Science and the Chinese Ministry of Science and Technology (Grant Nos. 2004CB720607 and 04-PSA-M-01).

References and Notes

(1) (a) Zhao, D.; Feng, J.; Huo, Q.; Melosh, N.; Fredrickson, G. H.; Chmelka, B. F.; Stucky, G. D. *Science (Washington, D.C.)* **1998**, *279*, 548. (b) Zhao, D.; Huo, Q.; Feng, J.; Chmelka, B. F.; Stucky, G. D. *J. Am. Chem. Soc.* **1998**, *120*, 6024.

(2) Taguchi, A.; Schüth, F. *Microporous Mesoporous Mater.* **2005**, *77*, 1.

(3) Groothaert, M. H.; Smeets, P. J.; Sels, B. F.; Jacobs, P. A.; Schoonheydt, R. A. *J. Am. Chem. Soc.* **2005**, *127*, 1394.

(4) Groothaert, M. H.; van Bokhoven, J. A.; Battiston, A. A.; Weckhuysen, B. M.; Schoonheydt, R. A. *J. Am. Chem. Soc.* **2003**, *125*, 7629.

(5) Li, Y.; Armor, J. N. *Appl. Catal., A* **1999**, *188*, 211.

(6) Aresta, M.; Armor, J. N.; Barteau, M. A.; Beckman, E. J.; Bell, A. T.; Bercaw, J. E.; Creutz, C.; Dinjus, E.; Dixon, D. A.; Domen, K.; Dubois, D. L.; Eckert, J.; Fujita, E.; Gibson, D. H.; Goddard, W. A.; Goodman, D. W.; Keller, J.; Kubas, G. J.; Kung, H. H.; Lyons, J. E.; Manzer, L. E.; Marks, T. J.; Morokuma, K.; Nicholas, K. M.; Periana, R.; Que, L.; Rostrup-Nielson, J.; Sachtler, W. M. H.; Schmidt, L. D.; Sen, A.; Somorjai, G. A.; Stair, P. C.; Stults, B. R.; Tumas, W. *Chem. Rev.* **2001**, *101*, 953.

(7) *Catalysis by Unique Metal Ion Structures in Solid Matrices*; Centi, G., Wichterlova, B., Bell, A. T., Eds.; NATO Science Series, II; Kluwer Academic Publishers: Dordrecht, The Netherlands, 2001; Vol. 13.

(8) Zhang, Y.; Drake, I. J.; Bell, A. T. *Chem. Mater.* **2006**, *18*, 2347.

(9) Bordiga, S.; Buzzoni, R.; Geobaldo, F.; Lamberti, C.; Giamello, E.; Zecchina, A.; Leofanti, G.; Petrini, G.; Tozzola, G.; Vlaic. G. *J. Catal.* **1996**, *158*, 486.

(10) Panov, G. I. *CATTECH* **2000**, *4*, 18.

(11) Pérez-Ramírez, J.; Kapteijn, F.; Mul, G.; Moulijn, J. A. *Chem. Commun.* **2001**, 693.

(12) Pérez-Ramírez, J.; Kapteijn, F.; Mul, G.; Moulijn, J. A. *Appl. Catal., B* **2002**, *35*, 227.

(13) Pérez-Ramírez, J.; Kumar, M.; Brückner, A. *J. Catal.* **2004**, *223*, 13.

(14) Wang, Y.; Zhang, Q.; Shishido, T.; Takehira, K. *J. Catal.* **2002**, *209*, 186.

(15) Han, Y.; Meng, X.; Guan, H.; Yu, Y.; Zhao, L.; Xu, X.; Yang, X.; Wu, S.; Li, N.; Xiao, F. *Microporous Mesoporous Mater.* **2003**, *57*, 191.

(16) Tuel, A.; Gontier, S. *Chem. Mater.* **1996**, *8*, 114.

(17) Berlier, G.; Zecchina, A.; Spoto, G.; Ricchiardi, G.; Bordiga, S.; Lamberti, C. *J. Catal.* **2003**, *215*, 264.

(18) Sun, K.; Zhang, H.; Xia, H.; Lian, Y.; Li, Y.; Feng, Z. C.; Ying, P.; Li, C. *Chem. Commun.* **2004**, 2480.

(19) Sun, K.; Xia, H.; Hensen E. J. M.; van Santen, R. A.; Li, C. *J. Catal.* **2006**, *238*, 186.

(20) Jia, J.; Pillai, K. S.; Sachtler, W. M. H. *J. Catal.* **2004**, *221*, 119.

(21) Lobree, L. J.; Hwang, I. C.; Reimer, J. A.; Bell, A. T. *J. Catal.* **1999**, *186*, 242.

(22) Hensen, E. J. M.; Zhu, Q.; Hendrix, M. M. R. M.; Overweg, A. R.; Kooyman, P. J.; Sychev, M. V.; van Santen, R. A. *J. Catal.* **2004**, *221*, 560.

(23) Zhu, Q.; Teeffelen, R. V.; van Santen, R. A.; Hensen, E. J. M. *J. Catal.* **2004**, *221*, 575.

(24) Hensen, E. J. M.; Zhu, Q.; van Santen, R. A. *J. Catal.* **2003**, *220*, 260.

(25) Marturano, P.; Drozdová, L.; Kogelbauer, A.; Prins, R. *J. Catal.* **2000**, *192*, 236.

(26) Hensen, E. J. M.; Zhu, Q.; Janssen, R. A. J.; Magusin, P. C. M. M.; Kooyman, P. J.; van Santen, R. A. *J. Catal.* **2005**, *233*, 123.

(27) Hensen, E. J. M.; Zhu, Q.; van Santen, R. A. *J. Catal.* **2005**, *233*, 136.

(28) Zhu, Q.; Mojet, B. L.; Janssen, R. A. J.; Hensen, E. J. M.; Grondelle, J. van; Magusin, P. C. M. M.; van Santen, R. A. *Catal. Lett.* **2002**, *81*, 205.

(29) Fujdala, K. L.; Drake, I. J.; Bell, A. T.; Tilley, T. D. *J. Am. Chem. Soc.* **2004**, *126*, 10864.

(30) Holland, A. W.; Li, G. T.; Shahin, A. M.; Long, G. J.; Bell, A. T.; Tilley, T. D. *J. Catal.* **2005**, *235*, 150.

(31) Nozaki, C.; Lugmair, C.; Bell, A. T.; Tilley, T. D. *J. Am. Chem. Soc.* **2002**, *124*, 13194.

(32) Li, Y.; Feng, Z.; Lian, Y.; Sun, K; Zhang, L.; Jia, G.; Yang, Q.; Li, C. *Microporous Mesoporous Mater.* **2005**, *84*, 41.

(33) Goldfarb, D.; Bernardo, M.; Strohmaier, K. G; Vaughan, D. E. W.; Thomann, H. *J. Am. Chem. Soc.* **1994**, *116*, 6344.

(34) Berlier, G.; Spoto, G.; Bordiga, S.; Ricchiardi, G.; Fisicaro, P.; Zecchina, A.; Rossetti, I.; Selli, E.; Forni, L.; Giamello, E.; Lamberti, C. *J. Catal.* **2002**, *208*, 64.

(35) Kumar, M. S.; Schwidder, M.; Grünert, W.; Brückner, A. *J. Catal.* **2004**, *227*, 384.

(36) Tuel, A.; Arcon, I.; Millet, J. M. M. *J. Chem. Soc., Faraday Trans.* **1998**, *94*, 3501.

(37) Bordiga, S.; Damin, A.; Bonino, F.; Ricchiardi, G.; Lamberti, C.; Zecchina, A. *Angew. Chem., Int. Ed.* **2002**, *41*, 4734.

(38) Bordiga, S.; Damin, A.; Bonino, F.; Ricchiardi, G.; Zecchina, A.; Tagliapietra, R.; Lamberti, C. *Phys. Chem. Chem. Phys.* **2003**, *5*, 4390.

(39) Ricchiardi, G.; Damin, A.; Bordiga, S.; Lamberti, C.; Spanò, G.; Rivetti, F.; Zecchina, A. *J. Am. Chem. Soc.* **2001**, *123*, 11409.

(40) (a) Nishimura, Y.; Hirakawa, A. Y.; Tsuboi, M.; Clark, R. J. H.; Hester, R. E. *Advances in Infrared and Raman Spectroscopy*; Heyden & Son: London, 1978. (b) Carey, P. R. *Biochemical Applications of Raman and Resonance Raman Spectroscopies*; Academic Press: New York, 1982 and references therein.

(41) Li, C. *J. Catal.* **2003**, *216*, 203.

(42) Li, C.; Xiong, G.; Xin, Q.; Liu, J. K.; Ying, P. L.; Feng, Z. C.; Li, J.; Yang, W. B.; Yang, Y. Z.; Wang, G. R.; Liu, X. Y.; Lin, M.; Wang, X. Q.; Min, E. Z. *Angew. Chem., Int. Ed.* **1999**, *38*, 2220.

(43) Yu, Y.; Xiong, G.; Li, C.; Xiao, F. S. *J. Catal.* **2000**, *194*, 487.

(44) Xiong, G.; Li, C.; Li, H.; Xin, Q.; Feng, Z. *Chem. Commun.* **2000**, 677.

(45) Zhang, W. H.; Lu, J.; Han, B.; Li, M.; Xiu, J.; Ying, P.; Li, C. *Chem. Mater.* **2002**, *14*, 3413.

(46) Yang, Q. H.; Wang, S. L.; Liu, J. Q.; Xiong, G.; Feng, Z.; Xin, Q.; Li, C. *Appl. Catal.* **2000**, *194*, 507.

(47) Li, C.; Xiong, G.; Xin, Q.; Liu, J. K.; Ying, P.; Feng, Z. *J. Phys. Chem. B* **2001**, *105*, 2993.

(48) Li, Y.; Zhang, W. H.; Zhang, L.; Wei, Z.; Yang, Q.; Feng, Z.; Li, C. *J. Phys. Chem. B* **2004**, *108*, 9739.

(49) Zhang, L.; Yang, Q.; Zhang, W. H.; Li, Y.; Yang, J.; Jiang, D.; Zhu, G.; Li, C. *J. Mater. Chem.* **2005**, *15*, 2562.

(50) Sing, K. S. W.; Everett, D. H.; Haul, R. A. W.; Moscow, L.; Pierotti, R. A.; Ronquerol, J. *Pure Appl. Chem.* **1985**, *57*, 603.

(51) Samanta, S.; Giri, S.; Sastry, P.; Mal, N.; Bhaumik, A. *Ind. Eng. Chem. Res.* **2003**, *42*, 3012.

(52) Szegedi, Á.; Kónya, Z.; Méhnb, D.; Solymár, E.; Pál-Borbély, G.; Horváth, Z. E.; Biró, L. P.; Kiricsi, I. *Appl. Catal., A* **2004**, *272*, 257.

(53) Xu, M.; Wang, W.; Seiler, M.; Buchholz, A.; Hunger, M. *J. Phys. Chem. B* **2002**, *106*, 3202.

(54) Kruk, D.; Nilsson, T.; Kowalewski, J. *Phys. Chem. Chem. Phys.* **2001**, *3*, 4907.

(55) Strijkers, G. J.; Mulder, W. J. M.; Heeswijk, R. B; Frederik, P. M.; Bomans, P.; Magusin, P. C. M. M.; Nicolay, K. *MAGMA* **2005**, *18*, 186.

(56) Parris, E. P. *J. Catal.* **1963**, *2*, 371.

(57) Emeis, C. A. *J. Catal.* **1993**, *141*, 347.